The toy tokamak system code D0FUS and its first applications: impact of B and confinement scaling law on power plant design

Timothé Auclair[1], Eric Nardon[1], Yanick Sarazin[1], Jean-François Artaud[1], Baptiste Boudes[1], Clarisse Bourdelle[1], Jean-Luc Duchateau[1], and Alexandre Torre[1]

[1]CEA, IRFM, F-13108 Saint-Paul-lez-Durance, France

Contact : timothe.auclair@cea.fr

Abstract

D0FUS is a new toy system code written in Python and designed to enable fast, extensive, and easily interpretable parameter scans. Inspired by the approach of Freidberg et al. [1], D0FUS computes the main plasma stability indicators as well as the associated radial build. The code's architecture and capabilities are reviewed, and its governing equations are presented. First results show possible viable designs at large aspect ratio, explore possible operations at high magnetic field and highlight the critical role of the energy confinement time scaling laws.

Keywords: System code, power plant design

1 Introduction

Partly driven by the arrival of new private companies in the field, one observes a trend towards less conservative designs of potential fusion power plants. In this evolving landscape, the need for fast and easily interpretable predictions regarding the feasibility of any proposed design gets reinforced. The D0FUS toy model system code presented in this paper aims at this objective for tokamaks. This approach is inspired by the compact and tractable approach of Freidberg et al. to Tokamak Power Plant (TPP) design [1] and builds upon as well as reuses elements from [2] and [3]. Last, because of its inevitable simplifying assumptions, it is meant as a complementary tool to more advanced system codes [4][5][6][7].

Sections 2 and 3 introduce the general principle and main assumptions of the code. Sections 4 and 5 deal respectively with radial build and plasma stability constraints. D0FUS benchmarks with existing TPP studies are presented in Section 6. Section 7 introduces the main output figure of D0FUS. Finally, Section 8 presents first applications of D0FUS, devoted in particular to the impact of B and the confinement scaling law on TPP design.

2 General principle of D0FUS

The code takes four quantities as main inputs: the fusion power P_{fus}, the maximum magnetic field in the inner leg of the Toroidal Field (TF) coils $B_{\max}$, and the major (R_0) and minor (a) radii of the plasma. By scanning these parameters, one may explore the operating space of potential TPPs. The latter is delimited by both plasma stability and radial build (is there enough space to fit all the systems on the high-field side?) constraints. D0FUS also computes figures of merit such as fusion gain Q, neutron flux, proxies for cost and divertor heat flux, etc.

3 Key assumptions

In addition to those described in the following sections, key D0FUS assumptions are the following:

• Only steady-state machines are considered. Pulsed machines may be addressed in future work.

• Like in [1] and [2], the volumetric averaged temperature is imposed. We choose a default value of $\bar{T} = 14$ keV (which maximizes $\langle\sigma v\rangle/\bar{T}^2$).

• Radiative losses are presently ignored.

• Three different models describing the relationship between the maximum plasma vertical elongation κ and the aspect ratio A are currently implemented in the code [8][9][10][11]. However, since it is not clear which model is most relevant, κ is set to a fixed value here. The triangularity δ is also a fixed input parameter.

4 Radial build

A sketch illustrating the radial build is shown in Fig. 1. The first two thicknesses (starting from the right) are inputs of the code, i.e. the plasma minor radius (a) and the thickness of the first wall, breeding blanket, neutron shield, vacuum vessel, and associated gaps (b). a is generally scanned in the range $\sim 0.2-3$ m. b is typically fixed at 1.2 m, following Section III.B in [1], but we note that a range of b from $\simeq 0.8$ to 2.2 m can be found in the literature, based on different envisaged technologies and assumptions [12][13] [14][15][16][17].

The thicknesses of the TF coils (c) and Central Solenoid (CS) (d) are calculated to withstand the mechanical loads (with a maximum Tresca stress set to 660 MPa) and to provide enough magnetic flux to ramp up the plasma current. The code currently allows for two configurations: wedging (the TF coils support each other and do not touch the CS) and bucking (the TF coils are mechanically supported by the CS). For the wedging case, a model similar to that from [1] is used for the TF coils, and the model for the CS is briefly described in Appendix A.2. Models for the bucking case are not used here except for the benchmark against ARC (see Section 6) and will be described in a future publication.

5 Plasma stability

The plasma stability domain is bounded by the kink, Troyon and Greenwald limits. Before giving the definition of

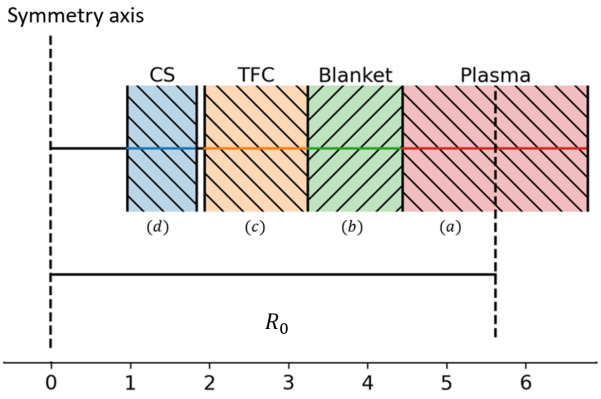

Figure 1: Sketch of a radial build output from D0FUS (wedging case)

the corresponding stability indicators in Subsection 5.4, we describe below the key preliminary steps to obtain the parameters appearing in these stability indicators.

5.1 The central magnetic field B_0

The magnetic field at the center of the plasma, B_0, is related to that at the inner leg of the TF coils, $B_{\max}$, by $B_0 = B_{\max}(R_0 - a - b)/R_0$ via Ampère's theorem.

5.2 Average plasma density and pressure

Considering a mixture of deuterium and tritium with equal densities n_D=n_T=n_{DT}, the fusion power reads (considering E_{fus}=E_N+E_α):

$$P_{fus} = E_{fus} \int_V n_{DT}^2 \langle \sigma v \rangle \, dV \tag{1}$$

Temperature and density profiles are parametrized as:

$$T = \bar{T}\,(1+\nu_T)\left(1-\rho^2\right)^{\nu_T} \qquad n_{DT} = \bar{n}_{DT}\,(1+\nu_n)\left(1-\rho^2\right)^{\nu_n} \tag{2}$$

with $\rho = r/a$ and volume-averaged quantities indicated by an overbar. As shown in Fig. 2, a rather peaked temperature profile and a nearly flat density profile are chosen: $\nu_T = 1.0$ and $\nu_n = 0.1$.

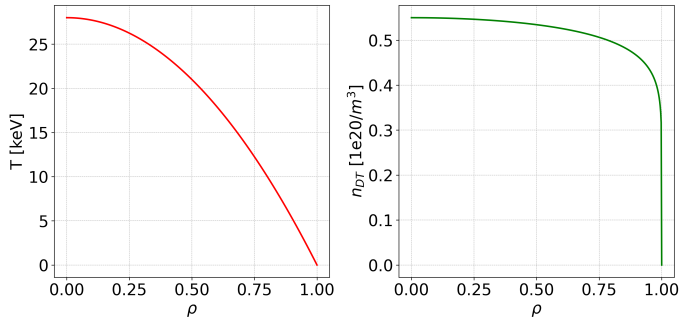

Figure 2: Typical temperature and density profiles used in D0FUS with $\bar{T}$=14keV and $\bar{n}_{DT} = 5 \times 10^{19} m^{-3}$

For $\langle \sigma v \rangle$, we use the accurate fit of Bosch and Hale [18], detailed in Appendix A.1. We then have an expression of P_{fus} that only depends on $\bar{n}_{DT}$ since $\bar{T}$ is fixed. Considering $dV = 2V_p \rho d\rho$ with $V_p = 2\pi^2 R_0 \kappa a^2$ the plasma volume, one can extract $\bar{n}_{DT}$:

$$\bar{n}_{DT} = \frac{1}{2}\sqrt{P_{fus}/[E_{fus}\pi^2 R_0 \kappa a^2 (1+\nu_n)^2 \int_0^1 (1-\rho^2)^{2\nu_n} \langle \sigma v \rangle \rho \, d\rho]} \tag{3}$$

We then aim to determine the electron density $\bar{n}$, taking into account helium dilution. To do so, we introduce the helium fraction $f_\alpha = \bar{n}_\alpha/\bar{n}$, allowing us to express $\bar{n}$:

$$\bar{n} = 2\bar{n}_{DT} + 2\bar{n}_\alpha = \bar{n}_{DT}\left(2 + \frac{4 f_\alpha}{1-2f_\alpha}\right) \tag{4}$$

We estimate f_α using Appendix B of [19], which is based on a fixed relationship between τ_E and τ_α (the confinement time of alpha particles), with the ratio $C_\alpha = \tau_\alpha/\tau_E$ set to a typical value of 5. Since τ_E is not initially known, f_α is initialized at a typical value of 5%. A convergence loop involving $\bar{n}$, τ_E, and f_α, as described in Appendix A.3, is then used to refine this value.

Since $p = (2-f_\alpha)nT$, the pressure profile simply reads $p = \bar{p}\,(1+\nu_p)\left(1-\rho^2\right)^{\nu_p}$ with $\nu_p = \nu_n + \nu_T$ and $\bar{p}$ given by:

$$\bar{p} = (2-f_\alpha)\,[(1+\nu_T)(1+\nu_n)/(1+\nu_p)]\,\bar{n}\bar{T} \tag{5}$$

5.3 Energy confinement time τ_E, plasma current I_p and fusion gain Q

The energy confinement time can be obtained through the power balance:

$$P_\alpha + P_{aux} \approx (1+5/Q)\,P_\alpha = (3/2)V_p\overline{p}/\tau_E$$
$$\Rightarrow \tau_E = 3\pi^2 R_0 a^2 \kappa \frac{E_{fus}}{E_\alpha P_{fus}} \overline{p} \frac{Q}{Q+5} \tag{6}$$

The plasma current needed to obtain such a τ_E can be deduced using a confinement scaling law [20][21]:

$$I_p = \left[\tau_E/(C_{SL} H R_0^{\alpha_R} a^{\alpha_a} \kappa^{\alpha_\kappa} \overline{n}^{\alpha_n} B_0^{\alpha_B} A^{\alpha_A} (P_\alpha + P_{aux})^{\alpha_P})\right]^{\frac{1}{\alpha_I}} \tag{7}$$

So far, the value of Q remains undetermined. To obtain it, one considers a steady-state reactor where the CS is dimensioned to drive the current during the ramp-up phase only. During the steady-state phase, the current is then a combination of bootstrap and non-inductively current. For the latter, we consider Lower Hybrid Current Drive (LHCD), which exhibits the largest efficiency in terms of generated current per injected power. The expressions of the boostrap and LHCD currents are the following:

$$I_b = 268\left(\frac{a^{5/2}\kappa^{5/4}\overline{p}}{\mu_0\sqrt{R_0}I_p}\right)\int_0^1 \frac{\rho^{5/2}(1-\rho^2)^{1/2}}{b_\theta}\,d\rho \tag{8}$$

$$I_{CD} = \frac{1.2P_{\mathrm{CD}}}{n_\parallel^2 R_0 \bar{n}} = \frac{1.2P_{fus}}{n_\parallel^2 R_0 \bar{n} Q} \tag{9}$$

These expressions are directly taken from Eqs. 31, 43 and 44 in [1] where the expressions of $n_\parallel$ and b_θ can be found.

With $I_p = I_B + I_{CD}$, Q becomes the only unknown and can be determined numerically by means of a convergence loop whose details are provided in Appendix A.3, yielding values for τ_E and I_p.

5.4 Stability indicators

With all necessary parameters now determined, we can calculate the plasma stability indicators, defined such that a value below unity indicates plasma stability.

• The kink stability indicator involves the edge safety factor q_* normalized to its critical value q_k (conservatively set to 2.5 in this paper, somewhat above the theoretical minimum of $\simeq 2$):

$$f_q = \frac{q_k}{q_*} = \frac{\mu_0 R_0 I_p q_k}{2\pi a^2 B_0 \left(\frac{1+\kappa^2}{2}\right)} \tag{10}$$

• The Troyon stability indicator involves the normalized beta β_N divided by its critical value β_T (set to 2.8% in this paper):

$$f_\beta = \frac{\beta_N}{\beta_T} = \frac{2\mu_0 \bar{p} a}{I_p B_0 \beta_T} \tag{11}$$

• The Greenwald stability indicator involves the average density $\bar{n}$ normalized by the Greenwald density n_G:

$$f_n = \frac{\bar{n}}{n_G} = \frac{\pi a^2 \bar{n}}{I_p} \tag{12}$$

6 Benchmark

In spite of its limitations, D0FUS is able to approximate machine designs produced with more advanced system codes. Table 1 presents a comparison to published steady-state designs. In this table, bold font indicates D0FUS output parameters, while light font corresponds to input parameters. Since the code has not yet been developed to account for pulsed configurations, no comparison with ITER or EU-DEMO is presented.

Overall, a reasonable agreement is observed in terms of B_0, I_p, $\bar{n}$, β_N, c (TF) and d (CS) thicknesses (no solution is found for the CS of ARC, probably because a model for a central insert inside the CS is presently not available in D0FUS). However, D0FUS appears optimistic regarding Q, likely due to relying on high-efficiency LHCD.

7 Output figures

In order to ease the exploration of the TPP parameter space, D0FUS produces output figures such as Fig. 3, which are constructed as follows. The four main D0FUS input parameters described in Section 2 create a 4D space to explore. Output figures display 2D slices of this space by scanning two input parameters while keeping the other two fixed. By default, R_0 and a are scanned at prescribed B_{max} and P_{fus}. Each position of this 2D space is colored according to the largest of the three plasma stability indicators, with green, red, and blue representing the kink, Troyon, and Greenwald indicators, respectively (eqs. 10,11 and 12). The plasma stability boundary is depicted by a dashed grey line. The black line within this stable plasma region is the boundary for viable radial build. Inside this viable space, iso-lines of a selectable parameter are shown in grey. Finally, iso-lines of an additional indicator are shown in white. In Fig. 3, I_p is shown in black and Q in white (up to 50, to avoid overloading the figure, and because the region of interest for a TPP lies specifically beyond 50), but other options comprise $\bar{n}$, β_N, neutron flux, proxies for machine cost or divertor heat flux, etc.

8 First results

8.1 General trends

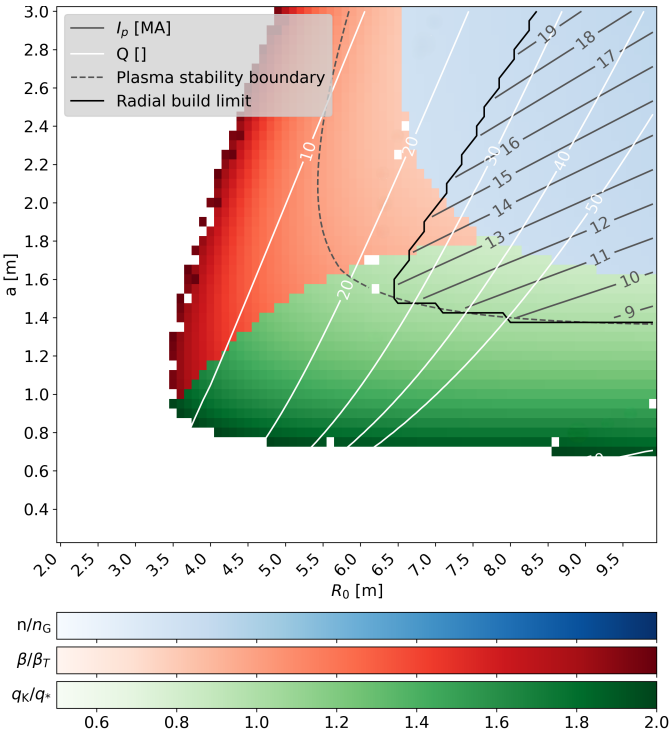

Figure 3: D0FUS scan on a and R_0 with B_{max}=12T and P_{fus}=2GW

Fig. 3 presents an illustrative scan on a and R_0 at fixed values of other parameters: P_{fus} = 2 GW, B_{max} = 12 T (representative of Low Temperature Superconductors, LTS), $\kappa = 2.1$, $\delta = 0.33$, $b = 1.2$ m. The confinement scaling law used is IPB98(y,2) with $H_{98} = 1$, and the machine is in wedging configuration.

This figure illustrates the general form of the TPP solution space. Regarding plasma stability, at small a, the kink limit restricts accessible solutions, while at small R_0, the Troyon limit generally applies. However, radial build is the most restrictive limit at small R_0.

Interestingly, at fixed R_0, it looks beneficial to reduce the minor radius a down to aspect ratios A much higher than usually considered ($\simeq 3$), both from the point of view of I_p and Q. Moving in this direction should also reduce the cost. To understand the reduction of I_p with a at fixed P_{fus} and R_0, we analyze the dependency of the various parameters with a: from the definition of P_{fus}, we see that the density $\bar{n}$ scales as $1/a$ (Eq. 3). Consequently, $\bar{p}$ also scales as $1/a$ according to Eq. 5. Neglecting variations of Q in Eq. 6, we infer that τ_E scales as a. Finally, using Eq. 7 and the dependencies described earlier, we find that I_p scales as $\left(a^{1+\alpha_n-\alpha_a}\right)^{1/\alpha_I}$ (here, the variation of B_0 with a is neglected due to its small exponent and limited evolution with a). Applying the IPB98(y,2) scaling law, we find an approximate dependence $I_p \propto a$, consistent with the trend observed in Fig. 3. However, important caveats apply to these interesting high A regions: first, confinement scaling laws for τ_E are probably less reliable for A significantly different from 3; second, these configurations lead to an increased neutron flux; third, achieving high κ may be more challenging at high A, finally, imposing an average temperature can force

Parameters	CFETR [DEMO-class] [2019]		K-DEMO [f_GW 1.1] [2015]		J-DEMO [2018]		ARC [2015]	
	Published [22]	D0FUS	Published [23-25]	D0FUS	Published [26-27]	D0FUS	Published [13]	D0FUS
P_fus [MW]	2192		3000		1420		525	
τ_pulse	Steady-State		Steady-State		Steady State		Steady-State	
Architecture	Wedging		Wedging		Wedging		Bucking	
R_0 [m]	7.2		6.8		8.5		3.3	
a [m]	2.2		2.1		2.42		1.13	
b [m]	1.5		1.7		~2		0.86	
TF: c [m]	**1.12**	**1.11**	**1.2**	**1.24**	**1.61**	**1.1**	**0.64**	**0.60**
σ_TF [MPa]	730		860		800		660	
CS: d [m]	**1.1**	**1.0**	**?**	**X**	**?**	**0.88**	**0.25**	**X**
σ_CS [MPa]	500		?	660	500		660	
κ	2.00		2.00		1.65		1.84	
B_max [T]	14.00		16.00		13.7		23	
B_0 [T]	**6.5**	**6.8**	**7.4**	**7.0**	**5.94**	**6.5**	**9.2**	**9.13**
P_aux [MW]	**77.81**	**69.9**	**128.2**	**43.8**	**83.6**	**30.8**	**38.6**	**9.0**
Q_plasma	**28.17**	**31.35**	**23.4**	**68.4**	**17.5**	**46.0**	**13.5**	**60.0**
I_p [MA]	**13.78**	**11.7**	**17.0**	**17.3**	**12.3**	**14.1**	**7.8**	**8.9**
H_98	1.42		1.17		1.31		1.8	
β_N [%]	**3.00**	**3.1**	**3.2**	**2.81**	**3.4**	**2.3**	**2.59**	**2.3**
C_alpha	?	5	?	5	?	5	?	5
<T> [keV]	~14		~17		16		14	
<n> [1e20/m^3]	**1.31**	**1.00**	**1.34**	**1.2**	**0.66**	**0.66**	**1.3**	**1.44**
n_GW [1e20/m^3]	**0.906**	**0.77**	**1.22**	**1.24**	**0.67**	**0.77**	**1.944**	**2.2**

Table 1: D0FUS benchmark on several designs

the temperature gradients to become very stiff in these low-a regions, potentially exceeding achievable limits.

8.2 Impact of magnetic field

Fig. 4 is the analogue of Fig. 3 at $B_{max} = 20$T instead of 12T, representative of high temperature superconducting coils. One can observe that, at fixed a and R_0, I_p depends weakly on B_{max}. This is due to the small exponent of B_0 in the confinement scaling law, e.g. $\alpha_B = 0.15$ in IPB98(y,2). It also appears that the plasma stability region is broadened at higher B_{max} thanks to the B_0 dependence of the kink and Troyon limits. In contrast, the radial build feasibility domain is shrunk, which motivates future studies on strategies to reduce the b, c and d thicknesses. It can also be noticed that Q is globally increased. This is due to the dependence of the LHCD efficiency on the cyclotron frequency.

Of course, whether compact high field TPPs are feasible also depends on the existence of solutions to handle the associated larger neutron flux and divertor heat flux. These aspects are left for future studies.

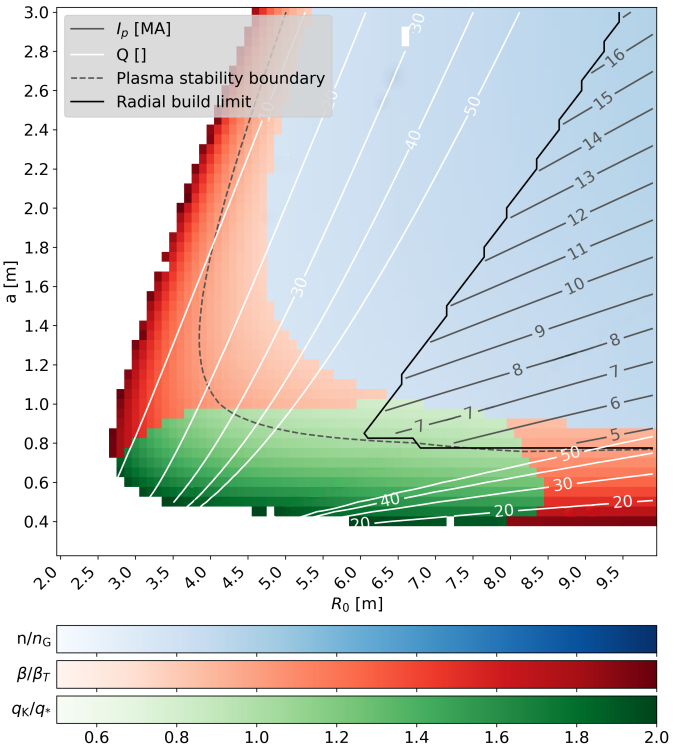

Figure 4: D0FUS scan on a and R_0 with B_{max}=20T and P_{fus}=2GW

8.3 Impact of confinement scaling law

An important further observation is the strong dependence of viable TPP parameter space on the confinement scaling law. For instance, Fig. 5 demonstrates that using ITPA20-IL [21] instead of IPB98(y,2) significantly reduces the plasma stability domain, as seen in comparison with Fig. 3. This is related to a larger requested I_p with ITPA20-IL, leading to kink and Troyon limit issues. Note also that Q remains below 20 within the plotted viable domain.

We also recognize and highlight that these scaling laws offer limited predictive accuracy for burning plasmas and

that enhanced efforts within the community on this topic are essential.

It is also worth mentioning that, unsurprisingly, D0FUS does not find any TPP solution of reasonable size when using an L-mode confinement scaling law.

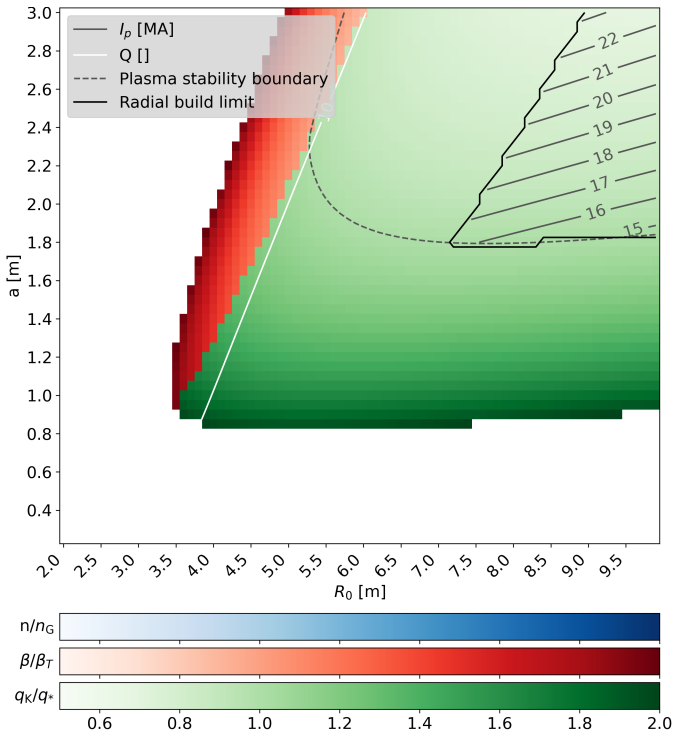

Figure 5: D0FUS scan on a and R_0 with B_{max}=12T and P_{fus}=2GW using ITPA20-IL instead of IPB98(y,2) used in Fig. 3

9 Conclusion

D0FUS is a new toy system code enabling fast and easily interpretable scans of the Tokamak Power Plant design space. Its first results suggest the existence of solutions at high-aspect-ratio with higher Q and lower I_p than conventional ($A \simeq 3$) solutions, although these are probably more challenging in terms of neutron flux and vertical control, among other possible caveats. The code also shows that increasing B_{max} affects TPP design mainly via improving plasma stability while making the radial build more constraining. Finally, D0FUS shows the strong impact of the confinement scaling law on the TPP design space.

Acknowledgements

This work is financially supported by the French government's "France 2030" initiative through the "ANR" (National Research Agency) in the framework of the SupraFusion PEPR Program and its SF-Plant research project.

A Appendices

A.1 $\langle \sigma v \rangle$ calculus

The fit used in D0FUS for the relationship between $\langle \sigma v \rangle$ (in m^3/s) and T (in keV) for the D-T reaction [28] is taken from [18]:

$$\langle \sigma v \rangle = c_1 \theta \left(\frac{\phi}{mc^2 T^3} \right)^{1/2} e^{-3\phi} \times 10^{-6} \tag{13}$$

where

$$\theta = \frac{T}{1 - \frac{T(c_2 + T(c_4 + T \cdot c_6))}{1 + T(c_3 + T(c_5 + T \cdot c_7))}} \quad \text{and} \quad \phi = \left(\frac{{B_G}^2}{4\theta} \right)^{1/3}$$

with

Symbol	Value
B_G (keV$^{1/2}$)	34.3827
mc^2 (rest mass in keV)	1124656
c_1	1.17302×10^{-9}
c_2	1.51361×10^{-2}
c_3	7.51886×10^{-2}
c_4	4.60643×10^{-3}
c_5	1.35000×10^{-2}
c_6	-1.06750×10^{-4}
c_7	1.36600×10^{-5}

Its maximum deviation is 0.35% for T in the range of 0.5 to 100 keV.

A.2 CS wedging model

In our model, the CS is treated as a single isotropic material whose properties are averaged over its steel and conductor (including superconductor, copper and cooling) components. The distribution between steel and conductor is characterized by a factor $\alpha_{CS} = \frac{V_{conductor}}{V_{total}}$, where $V_{conductor}$ and V_{total} represent respectively the volumes of conductor and total material, as illustrated in Fig. 6.

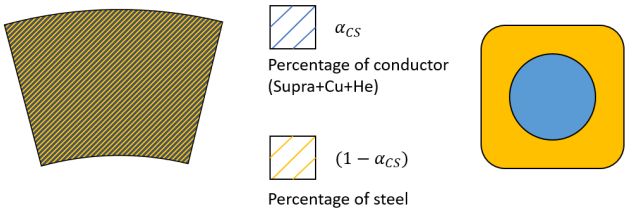

Figure 6: Illustration of the α_{CS} factor definition

The amount of steel is conservatively calculated to withstand all mechanical stresses without requiring structural support from the conductor. We then define $\sigma_{\text{Engineering}} = \sigma_{\text{CSmax}}(1 - \alpha_{\text{CS}})$ with σ_{CSmax} the mechanical limit of the chosen steel (a typical value is 660 MPa, neglecting fatigue since the machine is supposed to operate in steady-state), and $J_{Engineering} = J_{\text{CSmax}}\alpha_{\text{CS}}$ with J_{CSmax} the maximum current density allowed by the chosen conductor (a typical value is 50 MA/m^2, taken

from ITER 3Niobium-Tin cable, neglecting the effect of B on J).

We consider a conservative mechanical criterion, as we position ourselves at the inner radius of the CS $R_{\mathrm{CS}}^{\mathrm{int}}$, where the magnetic field is maximal, and assume no transfer of stress to other CS layers. The projected stress generated by the $J \times B$ force held through a vault effect can then be expressed as:

$$\sigma_{Engineering} = J_{Engineering} B_{CS} R_{\mathrm{CS}}^{\mathrm{int}} \tag{14}$$

The magnetic flux requirement, not considering any current drive assistance during the ramp up, is expressed as:

$$\Psi_{\mathrm{Init}} + \Psi_{\mathrm{Ramp\text{-}Up}} + \Psi_{\mathrm{Plateau}} = 2\Psi_{\mathrm{CS}} + \Psi_{\mathrm{PF}} \tag{15}$$

In Eq. 15:

• The flux consumption at plasma initiation is difficult to predict. In this paper we chose a probably conservative value: Ψ_{Init} = 20 Wb.

• The flux consumption to ramp up the plasma current is composed of two terms, respectively linked to the inductance and the resistance of the plasma:

$$\begin{aligned}\Psi_{\mathrm{Ramp\text{-}Up}} &= \Psi_{\mathrm{Ind}} + \Psi_{\mathrm{Res}} = L_{\mathrm{p}} I_p + C_{\mathrm{Ejima}} \mu_0 R_0 I_{\mathrm{p}} \\ &= \mu_0 R_0 I_{\mathrm{p}} \left(C_{\mathrm{Ejima}} + \frac{l_i}{2} + \log \frac{8R_0}{a\sqrt{\kappa}} - 2 \right)\end{aligned} \tag{16}$$

with the value of the normalized internal inductance l_i fixed by the user (0.5-0.9) or estimated using more refined models [29][30] and the Ejima constant C_{Ejima} fixed to a standard value of 0.45 [31] [32].

• As the plasma current is assumed to be entirely non-inductively driven, Ψ_{Plateau} is taken equal to 0.

• The CS flux can be expressed as:

$$\Psi_{\mathrm{CS}} = \frac{\pi B_{CS}}{3} \left((R_{\mathrm{CS}}^{\mathrm{ext}})^2 + R_{\mathrm{CS}}^{\mathrm{ext}} R_{\mathrm{CS}}^{\mathrm{int}} + (R_{\mathrm{CS}}^{\mathrm{int}})^2 \right) \tag{17}$$

• The contribution of the PF coils is approximated by calculating the vertical magnetic field and the corresponding flux as in [31]:

$$\begin{aligned}B_{\mathrm{vert}} &= \frac{\mu_0 I_{\mathrm{p}}}{4\pi R_0} \left(\beta_p + \frac{l_i - 3}{2} + \log \frac{8R_0}{a\sqrt{\kappa}} \right) \\ \Psi_{\mathrm{PF}} &= B_{\mathrm{vert}} \pi (R_0^2 - (R_{\mathrm{CS}}^{\mathrm{ext}})^2)\end{aligned} \tag{18}$$

with β_p approximated from [2], k_B the Boltzmann constant and L the length of the last closed flux surface:

$$\beta_p = \frac{4\bar{n} k_B \bar{T} L^2}{\mu_0 I_p^2}$$

We do not consider any contribution of B_{vert} within the CS (this explains the $R_0^2 - (R_{\mathrm{CS}}^{\mathrm{ext}})^2$ factor). Indeed, the CS will be sized to generate a maximum magnetic field that cannot be exceeded, including B_{vert}.

Finally, making use of Ampère's theorem, one can link the magnetic field inside the CS with its radius:

$$B_{CS} = \mu_0 J_{Engineering} (R_{\mathrm{CS}}^{\mathrm{ext}} - R_{\mathrm{CS}}^{\mathrm{int}})$$

Ensuring that only solutions satisfying $B_{CS} < B_{max}$ are selected, we then obtain a system of two equations with two unknowns (α_{CS} and $R_{\mathrm{CS}}^{\mathrm{int}}$), which can be solved numerically to determine the internal radius of the CS and the optimal distribution between conductor and steel.

A.3 Convergence loop on f_α and Q

Determining consistent values for Q and f_α with the rest of the model requires two nested numerical convergence loops, as illustrated in Fig. 7.

For f_α, we initialize a loops with a typical value of 5%, then compute the associated $\bar{n}$ and $\bar{p}$ from Eq. 4 and 5. This allows for the determination of the associated τ_E (Eq. 6) and f_α from Appendix B of [19] used as a new input.

For Q, the loop begins with a typical value of 100, calculates the associated τ_E, then the plasma current corresponding to this confinement time, and finally the current drive power needed to generate such a current, which yields to a new Q value, used as input for the next iteration.

In practice, the Q convergence loop is nested within the f_α loop, as Q influences the value of τ_E, this means that at each iteration of the convergence loop on f_α, a complete convergence on Q is achieved. Despite this, convergence remains very fast, requiring less than ten iterations on f_α and Q with respective relative convergence criteria of 10^{-3} and 10^{-2}. This ensures that generating a typical figure (e.g, Fig. 3) takes less than ten minutes on a standard office laptop.

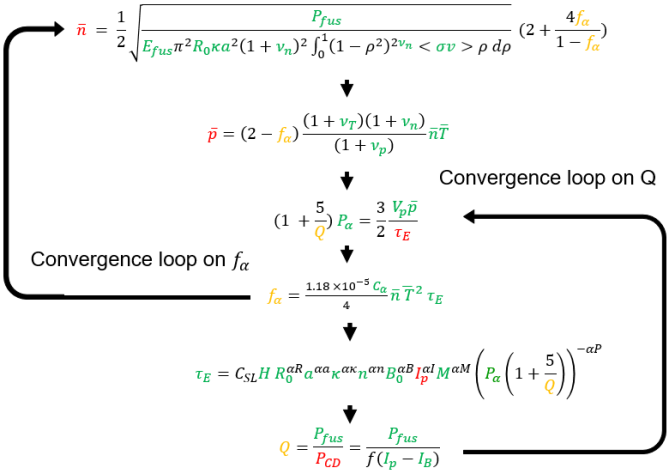

Figure 7: The two convergence loop, with, at each step, known values in green, determined parameters in red, and parameters evolving in the convergence loop in orange

References

[1] JP Freidberg, FJ Mangiarotti, and J Minervini. Designing a tokamak fusion reactor—how does plasma physics fit in? *Physics of Plasmas*, 22(7), 2015.

[2] Jean Johner. Helios: a zero-dimensional tool for next step and reactor studies. *Fusion Science and Technology*, 59(2):308–349, 2011.

[3] Yanick Sarazin, J-L Duchateau, X Garbet, P Ghendrih, R Guirlet, J Hillairet, B Pégourié, A Torre, and R Varennes. Impact of the aspect ratio on tokamak reactor design. In *IAEA FEC 2021-The 28th IAEA Fusion Energy Conference*, 2021.

[4] M Kovari, R Kemp, H Lux, P Knight, J Morris, and DJ Ward. "process": A systems code for fusion power

plants—part 1: Physics. *Fusion Engineering and Design*, 89(12):3054–3069, 2014.

[5] M Kovari, F Fox, C Harrington, R Kembleton, P Knight, H Lux, and J Morris. "process": A systems code for fusion power plants–part 2: Engineering. *Fusion Engineering and Design*, 104:9–20, 2016.

[6] M Coleman and S McIntosh. Blueprint: a novel approach to fusion reactor design. *Fusion Engineering and Design*, 139:26–38, 2019.

[7] Cédric Reux, Sébastien Kahn, L Zani, Bernard Pégourié, N Piot, Michal Owsiak, Giacomo Aiello, J-F Artaud, Arthur Boutry, Saied Dardour, et al. Demo design using the sycomore system code: Influence of technological constraints on the reactor performances. *Fusion Engineering and Design*, 136:1572–1576, 2018.

[8] Jeffrey P Freidberg, Antoine Cerfon, and JP Lee. Tokamak elongation–how much is too much? part 1. theory. *Journal of Plasma Physics*, 81(6):515810607, 2015.

[9] JP Lee, Antoine Cerfon, Jeffrey P Freidberg, and M Greenwald. Tokamak elongation–how much is too much? part 2. numerical results. *Journal of Plasma Physics*, 81(6):515810608, 2015.

[10] RD Stambaugh, LL Lao, and EA Lazarus. Relation of vertical stability and aspect ratio in tokamaks. *Nuclear fusion*, 32(9):1642, 1992.

[11] Matti Coleman. *An integrated design framework for future nuclear fusion power reactors*. PhD thesis, 2021.

[12] Daniel J Segal, Antoine J Cerfon, and Jeffrey P Freidberg. Steady state versus pulsed tokamak reactors. *Nuclear Fusion*, 61(4):045001, 2021.

[13] BN Sorbom, J Ball, TR Palmer, FJ Mangiarotti, JM Sierchio, P Bonoli, C Kasten, DA Sutherland, HS Barnard, CB Haakonsen, et al. Arc: A compact, high-field, fusion nuclear science facility and demonstration power plant with demountable magnets. *Fusion Engineering and Design*, 100:378–405, 2015.

[14] AQ Kuang, NM Cao, Alexander James Creely, Cody Andrew Dennett, J Hecla, Brian LaBombard, Roy Alexander Tinguely, Elizabeth Ann Tolman, Henry Hoffman, M Major, et al. Conceptual design study for heat exhaust management in the arc fusion pilot plant. *Fusion Engineering and Design*, 137:221–242, 2018.

[15] Gianfranco Federici, L Boccaccini, F Cismondi, M Gasparotto, Y Poitevin, and Italo Ricapito. An overview of the eu breeding blanket design strategy as an integral part of the demo design effort. *Fusion Engineering and Design*, 141:30–42, 2019.

[16] LV Boccaccini, L Giancarli, G Janeschitz, S Hermsmeyer, Y Poitevin, A Cardella, and E Diegele. Materials and design of the european demo blankets. *Journal of Nuclear Materials*, 329:148–155, 2004.

[17] A Li Puma, JL Berton, B Branas, L Bühler, J Doncel, U Fischer, W Farabolini, L Giancarli, D Maisonnier, P Pereslavtsev, et al. Breeding blanket design and systems integration for a helium-cooled lithium–lead fusion power plant. *Fusion Engineering and Design*, 81(1-7):469–476, 2006.

[18] H-S Bosch and Gerald M Hale. Improved formulas for fusion cross-sections and thermal reactivities. *Nuclear fusion*, 32(4):611, 1992.

[19] Y Sarazin, J Hillairet, J-L Duchateau, K Gaudimont, R Varennes, X Garbet, Ph Ghendrih, R Guirlet, B Pégourié, and A Torre. Impact of scaling laws on tokamak reactor dimensioning. *Nuclear Fusion*, 60(1):016010, 2019.

[20] ITER Physics Expert Group on Confinement Transport, , ITER Physics Expert Group on Confinement Modelling Database, , and ITER Physics Basis Editors. Chapter 2: Plasma confinement and transport. *Nuclear Fusion*, 39(12):2175–2249, 1999.

[21] Geert Verdoolaege, Stanley M Kaye, Clemente Angioni, Otto JWF Kardaun, Mikhail Maslov, Michele Romanelli, François Ryter, Knud Thomsen, JET Contributors, ASDEX Upgrade Team, et al. The updated itpa global h-mode confinement database: description and analysis. *Nuclear Fusion*, 61(7):076006, 2021.

[22] Ge Zhuang, GQ Li, J Li, YX Wan, Y Liu, XL Wang, YT Song, V Chan, QW Yang, BN Wan, et al. Progress of the cfetr design. *Nuclear Fusion*, 59(11):112010, 2019.

[23] Keeman Kim, K Im, HC Kim, S Oh, JS Park, S Kwon, YS Lee, JH Yeom, C Lee, GS Lee, et al. Design concept of k-demo for near-term implementation. *Nuclear Fusion*, 55(5):053027, 2015.

[24] TG Brown, P Titus, K Im, and K Kim. Design definition of the k-demo in-vessel blanket arrangement, blanket sector maintenance details and upper lever rm enclosure. *Fusion Engineering and Design*, 146:1203–1206, 2019.

[25] Ji Sung Kang, JM Park, L Jung, SK Kim, J Wang, CY Lee, DH Na, K Im, Y-S Na, and YS Hwang. Development of a systematic, self-consistent algorithm for the k-demo steady-state operation scenario. *Nuclear Fusion*, 57(12):126034, 2017.

[26] Kenji Tobita, Ryoji Hiwatari, Yoshiteru Sakamoto, Youji Someya, Nobuyuki Asakura, Hiroyasu Utoh, Yuya Miyoshi, Shinsuke Tokunaga, Yuki Homma, Satoshi Kakudate, et al. Japan's efforts to develop the concept of ja demo during the past decade. *Fusion Science and Technology*, 75(5):372–383, 2019.

[27] Hiroyasu Utoh, Yoshiteru Sakamoto, Hideaki Miura, Hitoshi Arakawa, Daisuke Echizenya, Takuya Matsuda, Mitsuru Hasegawa, and Kazuhiro Nomoto. Design study of superconducting coil system for ja demo. *Fusion Engineering and Design*, 202:114345, 2024.

[28] TA Heltemes, GA Moses, and JF Santarius. Analysis of an improved fusion reaction rate model for use in fusion plasma simulations. *Technická zpráva, Duben*, 2005.

[29] GL Jackson, TA Casper, TC Luce, DA Humphreys, JR Ferron, AW Hyatt, Edward Alan Lazarus, RA Moyer, TW Petrie, DL Rudakov, et al. Iter startup studies in the diii-d tokamak. *Nuclear Fusion*, 48(12):125002, 2008.

[30] A Salar Elahi and M Ghoranneviss. Determination of the plasma internal inductance and evaluation of its effects on plasma horizontal displacement in ir-t1 tokamak. *Journal of fusion energy*, 29:76–82, 2010.

[31] J-L Duchateau, P Hertout, B Saoutic, J-F Artaud, L Zani, and C Reux. Conceptual integrated approach for the magnet system of a tokamak reactor. *Fusion Engineering and Design*, 89(11):2606–2620, 2014.

[32] RD Stambaugh, VS Chan, AM Garofalo, M Sawan, DA Humphreys, LL Lao, JA Leuer, TW Petrie, R Prater, PB Snyder, et al. Fusion nuclear science facility candidates. *Fusion Science and Technology*, 59(2):279–307, 2011.